Comprehensive investigation of crystallographic, spin-electronic and magnetic structure of $(Co_{0.2}Cr_{0.2}Fe_{0.2}Mn_{0.2}Ni_{0.2})_3O_4$: Unraveling the suppression of configuration entropy in high entropy oxides

Abhishek Sarkar [a,b,*], Benedikt Eggert [c], Ralf Witte [b], Johanna Lill [c], Leonardo Velasco [b], Qingsong Wang [b], Janhavika Sonar [b,d], Katharina Ollefs [c], Subramshu S. Bhattacharya [d], Richard A. Brand [b,c], Heiko Wende [c], Frank M.F. de Groot [e], Oliver Clemens [a,f], Horst Hahn [a,b], Robert Kruk [b]

[a] KIT-TUD-Joint Research Laboratory Nanomaterials, Technical University Darmstadt, Darmstadt 64287, Germany
[b] Institute of Nanotechnology, Karlsruhe Institute of Technology, Eggenstein-Leopoldshafen 76344, Germany
[c] Faculty of Physics and Center for Nanointegration Duisburg-Essen (CENIDE), University of Duisburg-Essen, Lotharstr. 1, Duisburg 47057, Germany
[d] Nano Functional Material Technology Centre (NFMTC), Department of Metallurgical and Materials Engineering, Indian Institute of Technology Madras, Chennai 600036, India
[e] Inorganic Chemistry and Catalysis, Utrecht University, Universiteitsweg 99, CG Utrecht 3584, The Netherlands
[f] Institute for Materials Science, University of Stuttgart, Heisenbergstr. 3 Stuttgart 70569, Germany

ARTICLE INFO

ABSTRACT

High entropy oxides (HEOs) are a rapidly emerging class of functional materials consisting of multiple principal cations. The original paradigm of HEOs assumes cationic occupations with the highest possible configurational entropy allowed by the composition and crystallographic structure. However, the fundamental question remains on the actual degree of configurational disorder in HEOs, especially, in systems with low enthalpy barriers for cation anti-site mixing. Considering the experimental limitations due to the presence of multiple principal cations in HEOs, here we utilize a robust and cross-referenced characterization approach using soft X-ray magnetic circular dichroism, hard X-ray absorption spectroscopy, Mössbauer spectroscopy, neutron powder diffraction and SQUID magnetometry to study the competition between crystal field stabilization energy and configurational entropy governing the cation occupation in a spinel HEO (S-HEO), $(Co_{0.2}Cr_{0.2}Fe_{0.2}Mn_{0.2}Ni_{0.2})_3O_4$. In contrast to the previous studies, the derived complete structural and spin-electronic model, $(Co_{0.6}Fe_{0.4})(Cr_{0.3}Fe_{0.1}Mn_{0.3}Ni_{0.3})_2O_4$, highlights a significant deviation from the hitherto assumed paradigm of entropy-driven non-preferential distribution of cations in HEOs. An immediate correlation of this result can be drawn with bulk as well as the local element specific magnetic properties, which are intrinsically dictated by cationic occupations in spinels. The real local lattice picture presented here provides an alternate viewpoint on ionic arrangement in HEOs, which is of fundamental interest for predicting and designing their structure-dependent functionalities.

1. Introduction

The approach to design novel functional materials exploiting configurational disorder originated with the discovery of high entropy alloys (HEAs) [1]. The approach was recently extended to oxide systems [2–6]. High entropy oxides (HEOs) can be classified as single phase oxide solid solutions with the cationic sub-lattice/s populated by multiple elements in equiatomic or near-equiatomic proportions [5,7]. HEOs exhibit several appealing functionalities, which in many cases are the outcomes of the "entropy-based" design approach [3–5,8–13]. On the one hand, non-preferential, random occupation of the cations, most often resulting in the highest possible degree of configurational disorder allowed by the crystallographic structure, is considered common amongst the different classes of HEOs reported on until the present [5,7]. On the other hand, deviations from the complete disorder or non-preferential elemental occupation, possibly stemming from enthalpy effects, are inherently very difficult to study. A possibility or presence of short-range elemental correlations remain a subject of fundamental interest for all classes of high entropy materials. Recently, this

paradigm has been experimentally verified in the case of HEAs and medium entropy alloys (MEAs), where certain degree of chemical short range order or elemental fluctuations are now reported [14,15]. Importantly, a direct impact of the non-random chemical distribution leading to enhanced mechanical properties has been shown, prompting further research on enthalpy/entropy aspects in all HEAs/MEAs [14,15]. However, these kind of phenomena are largely unexplored in the case of HEOs and other groups of non-metallic high entropy materials. From a unit cell perspective, spinel type HEO (S-HEO) is an ideal candidate for evaluating the influence of configurational disorder on a fundamental level as extreme scenarios of either complete disorder or order are possible due to the low enthalpy barrier for cation anti-site mixing in spinels [16]. Nevertheless, unravelling the exact cationic distribution even in conventional spinel oxides remains challenging, which in the case of S-HEOs is further aggravated by the presence of multiple principal cations with possibilities of their different oxidation and spin states. However, such an endeavor is key to future applications, as the cationic occupations govern a majority of functional properties in spinels, a primary one being the magnetic property.

Since the first report in 2018 [17], S-HEOs have gained considerable research attention, which has resulted in several compositions exhibiting a variety of functional properties (see review articles [18,19]). Much research efforts have been devoted to the applied perspective of S-HEOs, such as investigation of the functional properties, discovery of new compositions and exploration of alternate synthesis routes. On the other hand, rigorous studies [20] focusing on the fundamental local structural and spin-electronic evaluation, which greatly influences their functional properties remains sparse. This study focuses on the initial S-HEO system, $(Co_{0.2}Cr_{0.2}Fe_{0.2}Mn_{0.2}Ni_{0.2})_3O_4$ [17], which has been extensively studied owing to its relevant magnetic, electrochemical and catalytic properties [17,21–33]. Previous reports on this system have always assumed a completely disordered structural model for $(Co_{0.2}Cr_{0.2}Fe_{0.2}Mn_{0.2}Ni_{0.2})_3O_4$, where all the cations are expected to equally and randomly occupy the octahedral (O^H) and tetrahedral (T^D) sites [17,21–29,31–33]. In a recent study, Cieslak et al. [30] used ^{57}Fe Mössbauer spectroscopy for the first time along with Korringa-Kohn-Rostoker (KKR)-coherent potential approximation (CPA) approach, where they observed certain degree of site preferences. Nevertheless, the proposed occupation model, $(Co_{0.05}Cr_{0.35}Fe_{0.35}Mn_{0.05}Ni_{0.2})$ $(Co_{0.275}Cr_{0.125}Fe_{0.125}Mn_{0.275}Ni_{0.2})_2O_4$, is still very close to the random configuration [30]. However, the experimental limitation for precisely determining the cation occupation in this study [30] was the use of Cu X-ray diffraction (XRD) and spectroscopy sensitive to one element only. The constituent transition metal (TM) cations have very close atomic scattering factors and cannot be easily distinguished in XRD, while ^{57}Fe Mössbauer spectroscopy is exclusively specific to Fe and does not provide information about any of the other cations. Moreover, ^{57}Fe Mössbauer spectroscopy was also performed in absence of an external magnetic field, which often makes it challenging to separate the effect of Fe occupying the T^D and O^H sites.

In this work, several element-specific techniques, such as hard and soft X-ray absorption near edge spectroscopy (XANES), soft X-ray magnetic circular dichroism (XMCD) and ^{57}Fe Mössbauer spectroscopy (both in presence and absence of an external magnetic field) have been used. These are complemented with neutron powder diffraction (NPD), XRD, transmission electron microscopy (TEM) and magnetometry, to unravel the details of ionic arrangements and magnetic structure of $(Co_{0.2}Cr_{0.2}Fe_{0.2}Mn_{0.2}Ni_{0.2})_3O_4$. Each of these techniques possess certain limitations due to the presence of several cations with close atomic and neutron/atomic scattering factors, multivalency and multisite occupations (i.e., overlap of O^H and T^D pre-edge transitions in *K*-edge XANES), mak-

ing it challenging to extract all the information individually from one technique. Hence, the combination of complementary characterization techniques becomes extremely critical in case of a complex scenario such as in S-HEO, as it substantially lowers the overall experimental inaccuracies that can arise from the limitation of the individual ones. The schematic in Figure 1, provides an overview of the comprehensive experimental protocol used in this study. The conclusions drawn from each set of characterization techniques and the limitations faced to provide the complete information of the S-HEO individually from these techniques are also highlighted in Figure 1. Consequently, in contrast to the existing reports on S-HEO, very strong preferences in the cation occupation resulting in the least possible configurational disorder allowed by the composition and crystal structure have been observed. Importantly, the broader objective of the study (Figure 1) is to provide a correlation between the long-range magnetic structure and element specific magnetic characteristics with the crystallographic structure and cation spin-oxidation states of $(Co_{0.2}Cr_{0.2}Fe_{0.2}Mn_{0.2}Ni_{0.2})_3O_4$.

2. Experimental Section

2.1. Synthesis

An aerosol based nebulized spray pyrolysis (NSP)[4] technique was utilized for synthesis of nanocyrstalline S-HEO. Aqueous based precursor solution was prepared by dissolving stoichiometric proportion of the nitrate salts of the corresponding metals in deionized water. The aerosol was formed using a piezo-driven nebulizer that was carried to the hot-wall reactor using N_2. The reactor was maintained at a temperature of 1050°C under a pressure of 900 mbar. The powders so formed were collected using a filter-based collector. The formed single-phase HEO after the NSP synthesis is nanocrystalline in nature. Hence, in order to obtain a sample representative of the bulk and as close as possible to the equilibrium ground state, the obtained powder was annealed at 1000°C for 10 hours in an air atmosphere with a ramp rate of 5°C per minute.

2.2. Structural, electronic and magnetic characterization

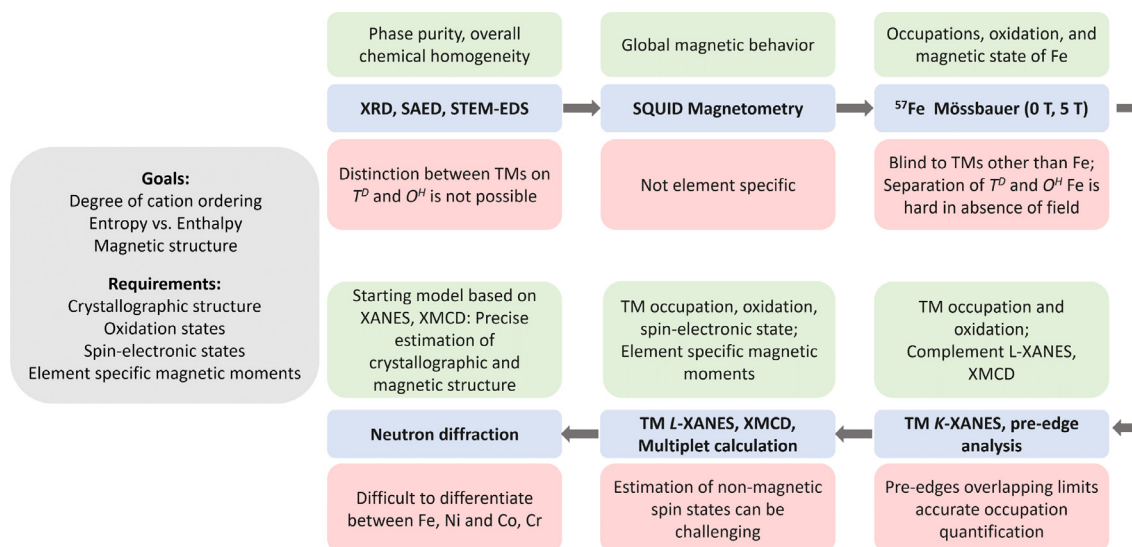1. **X-ray and neutron powder diffraction**
   High resolution X-ray diffraction (XRD). XRD patterns were recorded at room temperature, using a STOE Stadi P diffractometer, equipped with a Ga-metal jet X-ray source (Ga-Kβ radiation, 1.2079 Å). Patterns were collected between 10° and 90° with a step size of 0.05° at a scan rate of 4 s per step.
   Neutron powder diffraction (NPD): The time-of-flight (TOF) NPD pattern was measured on POWGEN at the Spallation Neutron Source (SNS) at the Oak Ridge National Laboratory. The sample was loaded into a vanadium can with a inner diameter of 6 mm, which was sealed with a copper gasket and aluminum lid. The measurement was performed at 300 K with neutrons of average wavelengths 0.8 Å, covering a d-spacing range of 0.48 - 10 Å.
   Rietveld analysis of the XRD and NPD patterns was done using TOPAS V.5.0[34]. The instrumental intensity distribution of the XRD and NPD instruments were determined empirically using reference scan of LaB$_6$ (NIST 660a) and Si, respectively. The microstructural parameters (crystallite size and strain broadening) were refined to adjust the peak shapes. Thermal displacement parameters were constrained to be the same for all atoms on a specific site. For oxygen, anisotropic displacement parameters were refined. For the determination of the magnetic structure, the reader is referred to Sec. 3.6.

2. **Transmission electron microscopy (TEM) and energy dispersive X-ray spectroscopy (EDX)**: Specimens for TEM and EDX

Phase purity, overall chemical homogeneity	Global magnetic behavior	Occupations, oxidation, and magnetic state of Fe
XRD, SAED, STEM-EDS	**SQUID Magnetometry**	**^{57}Fe Mössbauer (0 T, 5 T)**
Distinction between TMs on T^D and O^H is not possible	Not element specific	Blind to TMs other than Fe; Separation of T^D and O^H Fe is hard in absence of field

Goals:
Degree of cation ordering
Entropy vs. Enthalpy
Magnetic structure

Requirements:
Crystallographic structure
Oxidation states
Spin-electronic states
Element specific magnetic moments

Starting model based on XANES, XMCD: Precise estimation of crystallographic and magnetic structure	TM occupation, oxidation, spin-electronic state; Element specific magnetic moments	TM occupation and oxidation; Complement L-XANES, XMCD
Neutron diffraction	**TM _L_-XANES, XMCD, Multiplet calculation**	**TM _K_-XANES, pre-edge analysis**
Difficult to differentiate between Fe, Ni and Co, Cr	Estimation of non-magnetic spin states can be challenging	Pre-edges overlapping limits accurate occupation quantification

Fig. 1. The schematic represents the comprehensive experimental protocol used to achieve the picture of enthalpy/entropy balance and magnetic structure in the S-HEO. The limitations of the individual techniques to solely provide the full solution in the case of S-HEO are indicated in the light pink boxes, which indicate the necessity of the combined and cross-correlated experimental techniques used here. The conclusions that are drawn from each characterization set are highlighted in the light green boxes.

were prepared by dispersing the finely ground powders onto a standard carbon coated copper grid. A FEI Titan 80-300 aberration (imaging C_s) corrected TEM equipped with an EDS detector and a Gatan Tridiem 863 image filter operated at 300 kV was used to examine the specimens.

3. **Superconducting Quantum Interference Device (SQUID)**. Magnetic characterization was performed using a Quantum Design MPMS3 SQUID vibrating sample magnetometer (VSM). All magnetization measurements were done in VSM mode. Temperature dependent measurements between 5 and 380 K were performed following a zero-field cooled (ZFC) - field cooled (FC) protocol: the sample was cooled in zero magnetic field down to 5 K. Then the external field $\mu_0 H$ was applied and the magnetization was then measured during warming up to 380 K (ZFC branch). Subsequently, the magnetization was measured with the magnetic field applied from 380 K to 5 K (FC branch). Magnetic field dependent $M(\mu_0 H)$ measurements at different temperatures were also performed after cooling in zero magnetic field.

4. **Mössbauer spectroscopy**. ^{57}Fe Mössbauer spectroscopy both in absence ($H_{ext} = 0$ T) and presence ($H_{ext} = 5$ T) of external magnetic field was performed employing a ^{57}Co:Rh source in transmission geometry (bulk sample) using a triangular sweep of the velocity scale. As conventionally done, all center shifts are given relative to α-Fe at room temperature. A flow type cryostat operating with liquid He was used for low temperature measurements. The spectra are fitted using the WinNormos (from R.A. Brand, WISSEL) for Igor software.

5. **X-ray absorption near edge spectroscopy (XANES) and X-ray magnetic circular dichroism (XMCD)**
   XANES in the hard X-ray regime probes the K-edges of the transition metals (TM) corresponding to the $1s \rightarrow 4p$ transitions. Measurements were performed at beamline P65 (PETRA III, Hamburg) [35]. The S-HEO powder was pressed into a pellet, while the absorption measurements were performed in transmission mode at 10 K.
   XANES and XMCD in soft X-ray regime reveal the transition from $2p \rightarrow 3d$ corresponding to the $L_{2,3}$ edges of the TM cations and the related dichroic response of the $3d$ states. Measurements were performed at the UE46_PGM-1, BESSY II of the Helmholtz-Zentrum Berlin [36]. The measurements were con-

ducted at 4 K in an external magnetic field of 6 T. Unlike XANES in the hard X-ray regime, these measurements were not performed in transmission geometry. Instead, absorption signals were detected using a total electron yield technique. The samples were pressed onto an Indium foil to ensure electrical grounding. A broad feature corresponding to the In M_2 edge was observed at 700.5 eV. Muliplet calculations were performed with CRISPY and CTM4XAS programs [37,38].

3. Results

3.1. Initial structural characterization: XRD and TEM

The S-HEO crystallizes in a phase-pure spinel ($Fd\bar{3}m$) structure with lattice parameter $a = 8.3480(2)$ Å as revealed by the high resolution Ga metal-jet XRD and TEM micrograph shown in Supplementary Figure SI1a and SI1b, respectively. The negligible peak broadening in the XRD pattern indicates a microcrystalline nature of the sample with minimal microstrain effects. The presence of micrometer sized crystallites is further corroborated by the transmission electron microscopy (TEM) studies (Figure 2a). The energy dispersive X-ray spectra (EDS) acquired from the scanning TEM mode indicate a correct stoichiometry and the absence of phase segregation in S-HEO (Figure 2a). It should be noted that the elemental distinction between the T^D and O^H cations in the studied S-HEO is not possible from the XRD or the EDS mapping. Hence, from XRD, TEM and EDS analysis, information on the phase purity of the S-HEO along with its lattice parameter, microstructural features and overall chemical homogeneity can be reliably ascertained.

Often HEOs are investigated to check for the signature of entropy driven single phase stabilization. In addition to calorimetric studies, a case of a clear entropy driven phase stabilization is typically revealed by phase segregation at lower temperatures followed by reversible transition to single-phase at higher temperature, as is observed in rocksalt-HEOs [2]. Hence, low temperature heat treatments were also performed on S-HEO (Supplementary Figure SI2). Unlike entropy stabilized rocksalt-HEO, the XRD patterns indicate the stability of the single phase S-HEO even at lower temperatures making the effect of entropy in phase stability of S-HEO rather unclear.
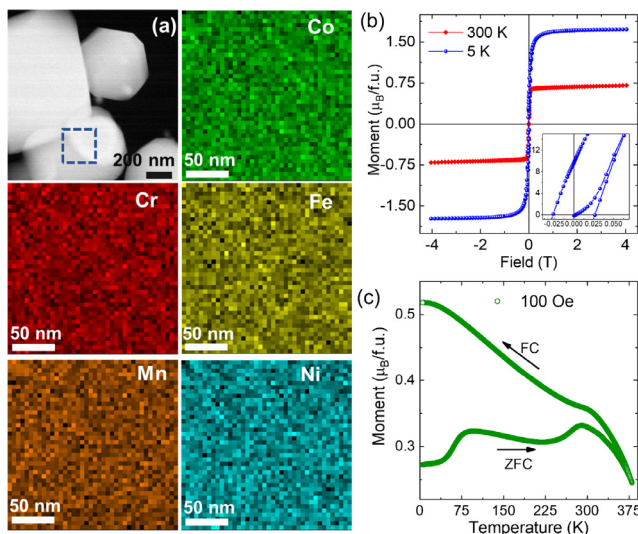
Fig. 2. (a) Scanning TEM micrograph and the corresponding elemental distribution maps for Co, Cr, Fe, Mn and Ni. (b) M-H plots of S-HEO at 300 K and 5 K with the inset showing the virgin curve measurement at 5 K. (c) ZFC-FC data in the M-T plot at 100 Oe indicate a series of magnetic transitions in S-HEO with the ferrimagnetic transition occurring above 380 K.

3.2. Bulk magnetic behavior: SQUID magnetometry

The field dependent magnetization measurements (M-H plots) at 300 K and 5 K are shown in Figure 2b. The M-H plot at 300 K exhibits an extremely soft magnetic behaviour with negligible coercivity (H_c). Nevertheless, the considerable saturation ($M_s = 0.67$ μ_B/f.u.) can be achieved in fields above 0.8 T, while $M_s = 1.73$ μ_B/f.u. and H_c of 230 Oe are observed at 5 K. These values are in agreement with those for bulk S-HEO prepared by solid state synthesis [22,30].

The temperature dependent magnetization measurements (M-T plots) from 5 - 380 K in a field of 100 Oe are shown in Figure 2c (and at 50 and 500 Oe in Supplementary Figure SI3). Considerable splitting between the field cooling (FC) and zero field cooling (ZFC) curves can be observed even at 380 K, which decreases for larger magnetic fields. This indicates that the magnetic transition temperature (T_c) of S-HEO is above 380 K, in agreement with $T_c \sim 425$ K reported by Musico et al. [22,30]. It is known that magnetic ordering can also effect the stability of certain phases, e.g. in α-Fe. However, such a scenario is unlikely in case of the S-HEO as the T_c (425 K or 152°C) is considerably lower than the synthesis temperature. Several inflection points can be seen in the M-T plots measured at 100 Oe and 50 Oe, similar to the observations in [22] where M-T was measured at 100 Oe. The features at around 242 K and 286 K are relatively weak and cannot be distinguished at 500 Oe or higher fields (Supplementary Figure SI3). Conversely, ZFC feature at $\sim$ 75 K is enhanced while measuring at higher magnetic field. The probable reasons for these magnetic features can be related to locally varying inter-site magnetic exchange interactions, whose strength can have different temperature dependencies. A consequence of this can be observed in spatial fluctuations of local magnetic order which might influence the movement of the domain walls in the external magnetic field. The virgin M-H magnetization measurements at different temperatures (see Supplementary Figure SI4) indicate a pinning type mechanism is prevalent in microcyrstalline S-HEO. Thus, the initial increase of the magnetization (ZFC) with temperature up to 75 K, observed in all measurements, can be attributed to the movement of magnetic domains governed by a (de)pinning of domain walls typical of many ferro/ferri-magnets. For a complete understanding of the
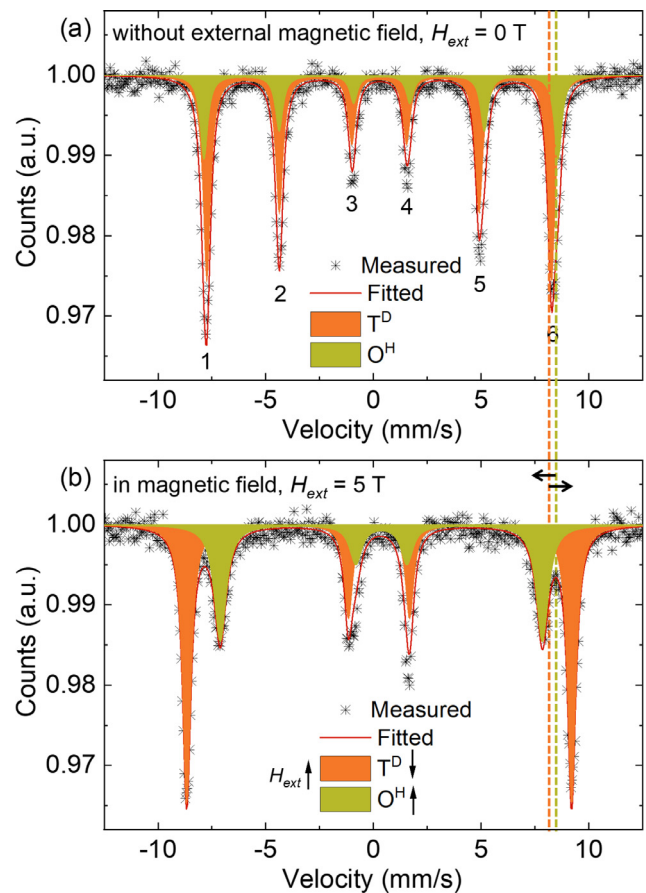
Fig. 3. Low temperature Mössbauer spectra of S-HEO (a) without magnetic field, i.e., 0 T (b) with an external magnetic field of 5 T. The orange sub-spectrum indicates the Fe^{3+} occupying the T^D sites, while the green one corresponds to the O^H sites. A clear distinction between the Fe^{3+} occupying the T^D and O^H sites can be observed in (b), while strong overlap of the features is observed in (a). The disappearance of the inner lines 2 and 5 in the (b) indicates a collinear arrangement of the Fe spins in both the sites.

exact nature of magnetization dynamics and switching, detailed microstructure studies and magnetic domain microscopy would be necessary, which is outside of the scope of this current study. Additionally, for further information on the ion-ion magnetic exchange interactions, support from theoretical studies (such as Monte-Carlo or density functional theory [39]) would be needed. Nevertheless, the aforementioned investigations confirm that the S-HEO sample studied here is phase pure and shows the prevalent magnetic features of bulk S-HEO.

3.3. ^{57}Fe Mössbauer spectroscopy in absence and presence of external magnetic field

^{57}Fe Mössbauer spectroscopy, in absence of an external magnetic field ($H_{ext} = 0$ T) as well as in presence of an external magnetic filed ($H_{ext} = 5$ T), was used to probe both the magnetic and charge state of Fe at a local level.

Figure 3 presents the low temperature Mössbauer spectra (with $H_{ext} = 0$ T and 5 T) of the S-HEO. The complete temperature series of $H_{ext} = 0$ T is presented in Supplementary Figure SI5a. A magnetic sextet is evident in all the spectra, supporting the magnetometry data that T_c is above room temperature. Supplementary Table SI1 includes detail of the hyperfine field (B_{hf}), isomer shift (δ) and the quadrupole line shift (2ϵ) for S-HEO at different temperatures. A deviation of the integral area ratio of the two outer sextet lines 1 and 2 to the innermost line 3 from the ideal values of 3:2:1 is

Table 1

Parameters obtained from fitting of the in-field (H_{ext} = 5 T) ^{57}Fe Mössbauer spectroscopy of S-HEO measured at 4.2 K, where B_{eff} is the effective hyperfine field, B_{hf} is the actual hyperfine field, δ is the isomer shift, 2ϵ is the quadrupole line shift, and I is the % of Fe on the respective sites. The canting angle $\Psi \approx 0$ (modulo π) for both T^D and O^H.

Site	B_{eff} (T)	B_{hf} (T)	δ (mm/s)	2ϵ (mm/s)	I (%)
T^D	55.4(2)	50.4(2)	0.38(0)	0.01(0)	68.1(6)
O^H	46.5(2)	51.5(3)	0.48(1)	0.01(0)	31.9(5)

observed in the room temperature spectrum Supplementary Figure SI5b, which can be ascribed to dynamic relaxation similar to that reported by Cieslak et al. [30]. Completely static sextets are used for fitting the 10 K spectrum (H_{ext} = 0 T) as shown in Figure 3a, which reflect the two different Fe environments, both corresponding to high spin (HS) Fe^{3+}. The green sub-spectrum, with a relative area of 27 %, corresponds to the Fe^{3+} occupying the O^H sites with, δ = 0.50(3) mm/s (with respect to α-Fe) and B_{hf} = 51.2(8) T. The orange sub-spectrum with a relative area of 73 %, isomer shift (δ) of 0.39(4) mm/s (with respect to α-Fe) and B_{hf} = 49.6(5) T corresponds to T^D-Fe^{3+}. The quadrupole line shift (2ϵ) is negligible in all cases below 225 K, i.e., after the static sextet is observed. These observed values are in close agreement with literature for Fe^{3+} occupying T^D and O^H sites [40,41]. The obtained amount of Fe occupying T^D is slightly higher than the observation from [30] corresponding to 60 %. However, the aforementioned investigation, as well as the one from Cieslak et al. [30], were carried out in absence of magnetic field (H_{ext} = 0 T). Thus, complete separation of the contribution from the T^D and O^H is challenging, due their similar B_{hf} values. Hence, in this study, in-field ^{57}Fe Mössbauer spectroscopy with an external magnetic field (H_{ext}) of 5 T applied parallel to the γ-rays at 4.2 K was additionally employed and the results are presented in Figure 3b.

In-field ^{57}Fe Mössbauer measurements are extremely precise in separating the Fe-site occupancies in the case of spinels, due the antiferromagnetic coupling between the O^H and T^D sub-lattices [42]. Consequently, Figure 3b shows two well-resolved outer lines compared to the Figure 3a. Since the hyperfine field in ^{57}Fe is antiparallel to the atomic moment, the H_{ext} of 5 T gets subtracted from the B_{hf} at the O^H-site, i.e., the direction of the primary magnetization of S-HEO. Conversely, the H_{ext} = 5 T is added to B_{hf} at the T^D-site i.e., originally anti-parallel to the net magnetization of the S-HEO. The details of the hyperfine parameters obtained from in-field ^{57}Fe Mössbauer measurement are presented in Table 1. It can be observed that actual B_{hf} obtained from the in-field measurement are in close agreement with ones to the estimated from fitting of the Mössbauer spectra measured in absence of field (H_{ext} = 0 T), Figure 3b. As expected, the isomer shifts (δ) of Fe^{3+} on either sites obtained from H_{ext} = 5 T (Table 1) match with the values obtained from the H_{ext} = 0 T measurement. The relative occupation of Fe, estimated from the well-resolved in-field ^{57}Fe Mössbauer spectra, indicates a 1:2 ratio of Fe^{3+} on O^H:T^D, Table 1.

Apart from the visible shift in the B_{hf}, another distinct difference between Figure 3a and Figure 3b is the almost complete disappearance of 2nd and 5th inner line in the case of H_{ext} = 5 T. This information is intimately related to the magnetic structure and the alignment of the (Fe) spins in the system. Intensity of the 2nd and 5th lines of the sextet in an in-field measurement depends on the square of the cosine of the canting angle Ψ ($\cos^2(\theta)$), which can be defined as the angle between the direction of the effective hyperfine field (B_{eff}) and the direction of $H_{ext} \parallel \gamma$-ray. The absence of the 2nd and 5th lines in S-HEO dictates that the Ψ for both O^H and T^D is close to 0° (or 180°, modulo π). Note that this extremal value indicates that all moments are parallel or antiparallel to the γ-ray

direction. This indicates a Néel-type collinear spin arrangement in S-HEO, similar to bulk $NiFe_2O_4$ [42]. However, unlike $NiFe_2O_4$ the collinearity of the spins is not intuitive in S-HEO, as the presence of multiple cations often leads to non-collinear spin arrangements in other classes of HEOs [8].

Thus, Mössbauer spectroscopy provides a first evidence of a Néel-type ferrimangetic structure along with substantial inversion and highly preferential cationic distribution in $(Co_{0.2}Cr_{0.2}Fe_{0.2}Mn_{0.2}Ni_{0.2})_3O_4$.

*3.4. TM K-edge XANES and pre-edge analysis*

Figure 4a-e present the XANES ($\mu(E)$) and the first order derivative ($d\mu(E)/dE$) of transition metal (TM) K-edges measured in transmission mode on a pellet sample, hence, probing the bulk of the system. The background corrected integrated intensity of the pre-edge feature in TM K-edges provides precious information about the site occupancy [43,44]. Typically, the integrated pre-edge intensity of a given 3d TM cation is larger in the T^D coordination than that of O^H coordination, due to negligible $d-p$ hybridization in the latter. However, in comparing different TMs, the electronic configuration of 3d state must also be considered.

The fine structure of the K-edge XANES spectrum of Co (Figure 4a) along with the strong pre-edge feature centering at 7709.6 eV, closely corresponds to Co^{2+} in a T^D environment [45]. The edge energy of 7718 eV and the features of the $d\mu(E)/dE$ also lead to the same conclusion [45,46]. However, a fraction of Co^{3+} is likely, hinted by the intensity ratio of the peaks centered at 7718 eV and 7722 eV observed in the $d\mu(E)/dE$ feature of Co K-edge XANES (Figure 4a) [46]. $L_{2,3}$-edge XANES and XMCD provide further insight into the charge and occupancy of Co, which will be discussed later. The spectral features of the Cr K-edge XANES (Figure 4b), $d\mu(E)/dE$ and edge energy (6007.1 eV) closely resemble those found for Cr^{3+} in O^H, as is observed in normal $ZnCr_2O_4$ spinel and other Cr containing oxides [47–49]. Although the pre-edge features are less intense compared to Co or Fe, the two peaks, a narrow one centered at 5986.6 eV and a broad one centered at 5991.7 eV, are distinct. These are indicative of the $1s \rightarrow 3d$ electric quadrupolar transitions, for Cr^{3+} in an O^H coordination [48]. It should be noted that a part of the broad pre-edge feature at 5991.7 eV can additionally stem from non-local transitions [50]. The results obtained here for Cr (also for Ni and to some extent for Fe, see below) are similar to what has been observed from the K-XANES study on another S-HEO composition, $(Co,Mg,Mn,Ni,Zn)(Al,Co,Cr,Fe,Mn)_2O_4$ [20]. For Fe, the edge energy (7123.5 eV) in the K-edge XANES (Figure 4c) along with the line shape and the peak position of the $d\mu(E)/dE$ closely resembles that of the 3+ ferrites, where Fe occupies both T^D and O^H sites [51,52]. The background subtracted pre-edge can be best fitted using a bimodal distribution with the dominant feature corresponding to the T^D geometry centering around 7113.5 eV along with a secondary peak stemming from the O^H occupancy centering around 7115 eV. However, an accurate estimation of the Fe occupancy solely from K-edge XANES is not reliable as it is difficult to distinguish the weak O^H contribution from the strong T^D transition. Nevertheless, the support from Mössbauer spectroscopy and $L_{2,3}$- XANES and XMCD (discussed later) provide a precise estimate of the Fe occupancy. Mn K-edge XANES (Figure 4d), is the most challenging spectrum where the support from the $L_{2,3}$-edge XANES and XMCD becomes more important. From the K-edge XANES analysis, we conclude that Mn is present predominantly in a 3+ oxidation state in O^H coordination [53]. The primary reasoning behind assigning the O^H occupancy relies on the fact that despite having fewer d electrons, the integrated intensity of the pre-edge feature (centering at 6539.7 eV) is significantly lower in magnitude compared to Fe and Co. A closer inspection of the line
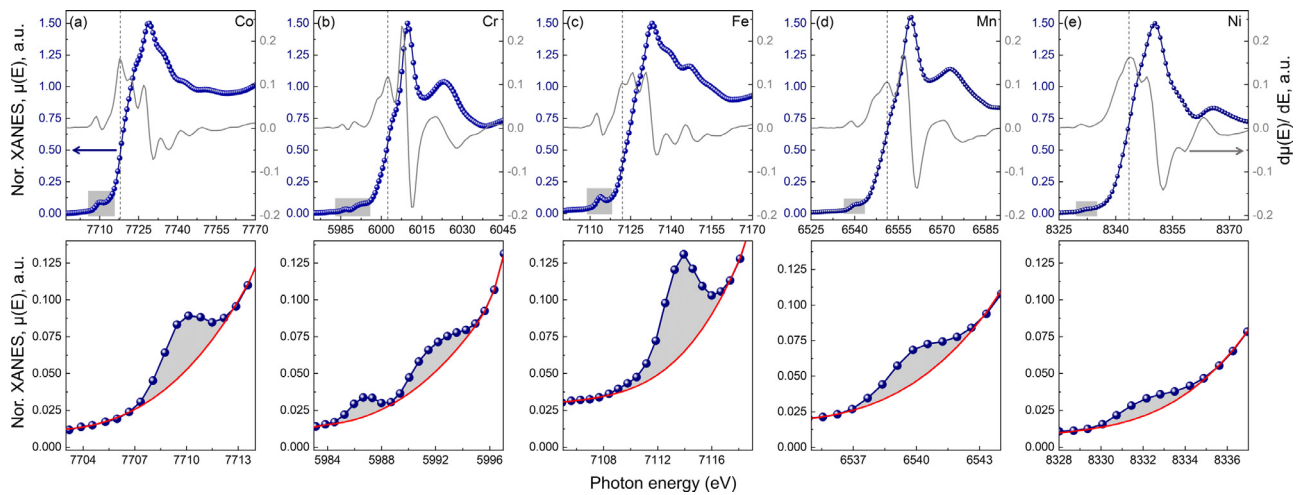
Fig. 4. The XANES spectra, $\mu(E)$ (blue), the first order derivative, $d\mu(E)/dE$ (grey) and the integrated intensity of the pre-edge region (bottom) at the TM K-edges of S-HEO. Cr, Mn and Ni exclusively occupy the O^H sites, Co occupies the T^D site and Fe occupies both with predominant T^D occupancy.
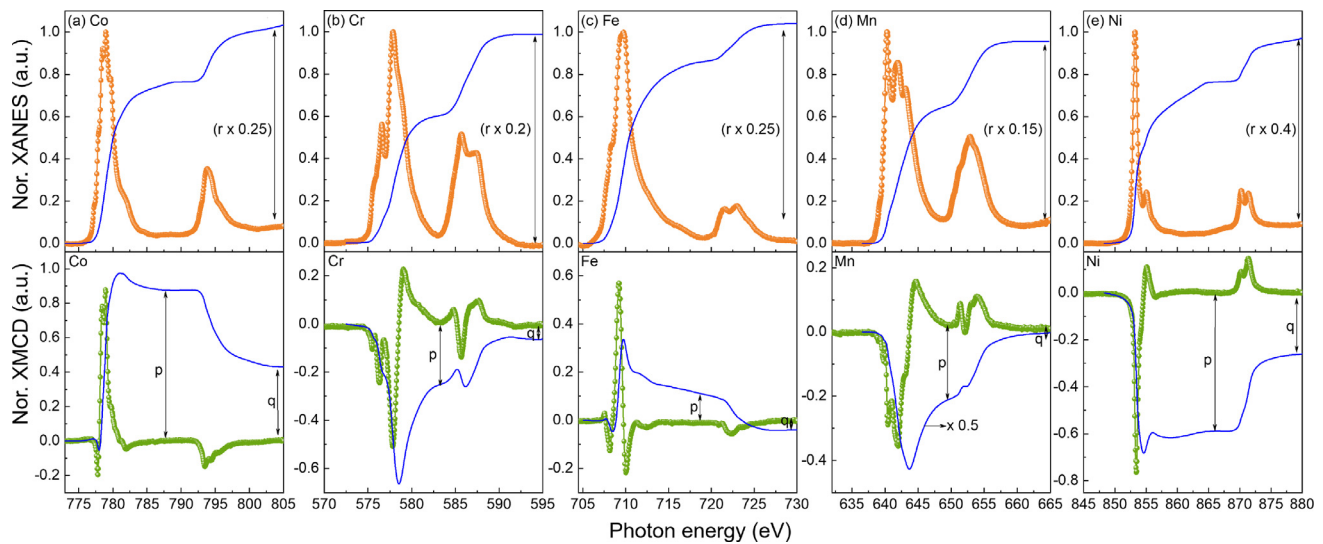
Fig. 5. XANES (upper, orange) and XMCD (lower, green) spectra at the TM $L_{2,3}$ edges of S-HEO measured with an external field of 6 T. The r is the integration over the XANES spectra, while p and q are the integration of the L_3 edge and $L_3 + L_2$ edges of the XMCD spectra. The magnitude and the sign of p in the XMCD spectra provide an indication about the elemental occupation, the negative p indicates predominant occupation parallel to the applied field, i.e., O^H occupation in S-HEO, while vice-versa indicates the T^D occupation.

shapes and the peak positions in the $d\mu(E)/dE$ (Figure 4d) further support a conclusion that Mn^{3+} predominates [53,54]. However, a small fraction of Mn^{2+} or Mn^{4+} cannot be excluded [53,54]. The K-edge XANES of Ni (Figure 4e) is in good agreement with those found in NiO and inverse $NiFe_2O_4$ indicating the presence of Ni^{2+} solely on the O^H sites [52,55]. The weak pre-edge feature and the edge energy of 8344 eV further substantiate this finding [20]. Hence, from the analysis of the K-edge XANES, it can be concluded that the S-HEO exhibits substantial preferences in the cation occupations. However, as discussed earlier (and shown in Figure 1), the overlapping of these pre-edge features, makes it challenging to accurately estimate cation occupations, especially in the case of Co, Fe and Mn. Thus, $L_{2,3}$-edges XANES, XMCD and NPD have been utilized in order to synergistically better estimate the occupations.

3.5. TM $L_{2,3}$-edges XANES and XMCD

Next, we evaluate the $L_{2,3}$-edges XANES and XMCD data which are presented in Figure 5. Owing to the antiparallel coupling be-

tween the T^D and O^H sites in spinels, the shape and direction of XMCD spectra on the $L_{2,3}$-edges provide comprehensive information about the occupation, oxidation and spin-electronic state of the constituent elements. In addition, XMCD sum rules [56,57] offer the possibility to estimate the element specific spin (m_S), orbital (m_L) and total (m_{tot}) moments (Supplementary Eqn. 1). The moments, m_S, m_L, m_{tot} are given in μ_B/atom (Supplementary Table SI2). The effective magnetic moment (m_{eff}) in μ_B/f.u. of the S-HEO is the $\sum m_{tot} \times 0.6$. It should be noted that for the $3d$ TM cations, sum rules are more reliable for iron and elements with atomic number above it, where the spin-orbit splitting, i.e., the distance between the L_3 and L_2 is considerable [58,59]. Hence, in S-HEO, the inaccuracies in the moments estimated from the sum rules for Fe, Co and Ni are comparatively smaller, which typically arise only from the background corrections affecting the area defined under the XANES spectra. For Cr and Mn, the inaccuracies are larger [58,59]. Nonetheless, even for Cr and Mn the sum rules are often used to provide a rough estimate and relative orientation of m_S and m_L [60–62]. Here, we utilize multiplet calculations, in addition, for a more precise evaluation of the $L_{2,3}$ XANES and XMCD
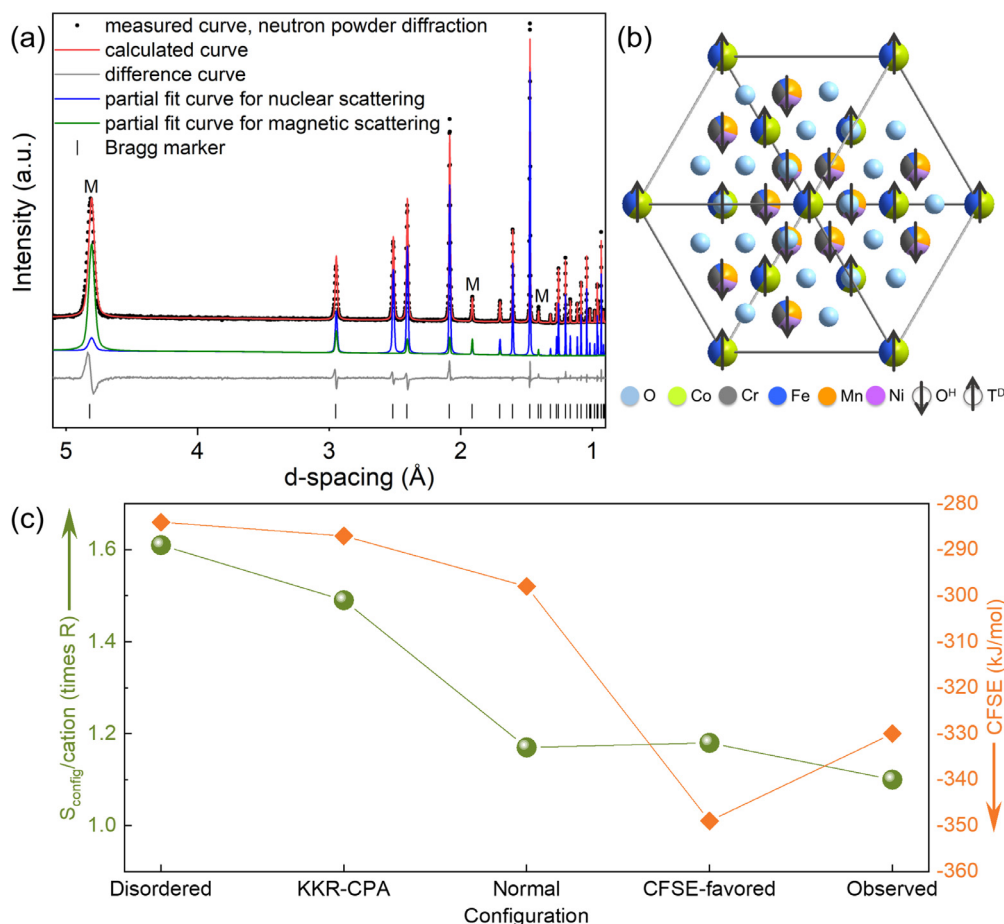
Fig. 6. (a) Neutron powder diffraction of S-HEO, where the reflections indicated by M are the ones strongly affected by the magnetic ordering. (b) Schematic of crystallographic and magnetic structure of S-HEO, along [111] (parallel projection). (c) The configurational entropy (S_{config}) and enthalpy (CFSE) for different possible occupational models of S-HEO are schematically compared. It should be noted that the S_{config} is presented independent of temperature, i.e. in units different from the CFSE.

spectra, which are presented in the Supplementary Figure SI6a-e and Supplementary Table SI3.

The $L_{2,3}$-edge XANES spectrum (Figure 5a) of Co in S-HEO appears to be a mixture of the 2+ and 3+ oxidation states, with clear predominance of the 2+ oxidation state as was also concluded from the K-edge XANES. The XMCD spectrum (Figure 5a) is nearly identical to high spin (HS)-Co^{2+} in T^D coordination ($3d^7$: e^4 t_2^3 ↓) [63]. It should be noted that all the spin states are presented with respect to the magnetization and the applied field. The additional presence of Co^{3+} contributions on the T^D site cannot be ignored. Hence, in combination with K-edge XANES and its first derivative, it can be estimated that roughly 60 % of Co in HS-Co^{2+} and 40 % of Co in HS-Co^{3+} are present in S-HEO. It is important to note that the intense and positive L_3 edge (p) in the XMCD (Figure 5a) almost completely rules out any possible magnetic Co O^H occupation. Another possibility, i.e., the presence of low spin (LS)-Co^{3+} ($3d^6$: t_{2g}^6) on the O^H, for which m_S is zero (therefore no XMCD signature), can also be discarded because it will then lower the overall m_{tot} for Co significantly. Further, the addition of Co on the O^H site worsens the neutron powder diffraction (NPD) fit that will be discussed later. Hence, the only likely possibility is the presence of HS-Co^{3+} on the T^D site $3d^6$: e^2 ↓ e^1 ↑ t_2^3 ↓, which also supports the high negative value of the Co-m_{tot} or m_S (Supplementary Table SI3). The multiplet calculation also indicates a predominance of Co^{2+} and the fit with 60 % HS-Co^{2+} and 40 % HS-Co^{3+} is shown in Supplementary Figure SI6a and Table SI3. A good match between the experimental and fitted XANES and XMCD fine structure could

be obtained, supporting the presence of the two sub-spectra. Importantly, the presence of Co solely in T^D is affirmed. In addition, the overall oxidation state of Co is estimated to be 2.4+. However, an inaccuracy of 2.4+ ± 0.2, but mostly slightly more Co^{2+} can be expected. This inaccuracy can plausibly be the reason for the width misfit in the calculated XMCD spectra (Supplementary Figure SI6a).

In the case of Cr (Figure 5b), the XANES spectrum, especially the line shape and the relative peak intensities closely match Cr^{3+} [61,64]. Likewise, the fine structures of the XMCD spectra along with the highly negative p (Figure 5b) and therefore, high and positive m_{tot} (Supplementary Table SI2) as a consequence, resemble the occupation of Cr^{3+} on the O^H sites with a HS electronic configuration: $3d^3$, t_{2g}^3 ↑ [61,64]. The result is further supported by the good agreement of the multiplet calculations with the experimental data, as shown in Supplementary Figure SI6b and Table SI3.

The spectral features of the Fe $L_{2,3}$ XANES and XMCD measurements (Figure 5c), specifically the peak at 708 eV in L_3 XANES and significantly low value of m_L/m_S (Supplementary Table SI2) are in good agreement with the 3+ oxidation state [65]. This further reinforces the conclusions reached for the oxidation state from Mössbauer spectroscopy and K-edge XANES. Focusing on the L_3 XMCD spectra of Fe, three distinct peaks can be observed which indicate antiferromagnetic coupling between the cationic sub-lattices. The intense positive peak at around 709 eV corresponds to the high spin (HS) T^D Fe^{3+} ($3d^5$: e^2 ↓ t_2^3 ↓), while the two minor peaks at 708 and 710 eV correspond to the O^H HS Fe^{3+} ($3d^5$: t_{2g}^3 ↑ e_g^2 ↑) [61]. The experimental XANES and XMCD spectra can be ad-

equately fitted using multiplet calculations for $\sim$33 % Fe^{3+} in O^H and $\sim$67 % Fe^{3+} in T^D as shown in Supplementary Figure SI6c. This quantitative finding is in close agreement with in-field Mössbauer analysis (Table 1). The m_S, m_L and m_{tot} for Fe obtained from the sum rules and multiplet calculations are listed in Supplementary Table SI2 and Supplementary Table SI3. The high negative value of m_{tot} indicates that Fe is predominantly aligned anti-parallel to the net magnetization, i.e., on the T^D.

For Mn, the XMCD and the highly negative p feature strongly indicate that Mn exclusively occupies the O^H sites (Figure 5d) [62,66]. In addition, almost complete quenching of the orbital moment of Mn can be concluded from the negligible m_L/m_S (Supplementary Table SI2). The $L_{2,3}$ XANES appears similar to a predominant of the 3+ oxidation state with a small fraction of 2+ resulting in the initial L_3 feature at 640 eV [66]. The line shape of the XMCD spectrum largely resembles Mn^{3+} ($t_{2g}^3 \uparrow e_g^1 \uparrow$) on the O^H site. Any presence of Mn^{2+} on T^D can be discounted given that its $3d^5$ electronic configuration would have led to an intense XMCD positive peak aligned anti-parallel to the applied field [67]. On the contrary, the related L_3 XMCD feature (640.4 eV) arising from Mn^{2+} exhibits a maximum in the negative direction (moment parallel to the external field). The multiplet calculation is challenging for Mn [59], due to the Jahn-Teller effect of Mn^{3+} on the O^H site. As can be observed in Supplementary Figure SI6d, the feature arising from the O^H Mn^{2+} (640.4 eV) can be readily fitted using the multiplet calculation. A strong intensity mismatch for the other features, especially the one at 642 eV, arising from the Mn^{3+} can be observed. Nevertheless, the corresponding XMCD features for all the L_3 XANES results are always parallel to the applied magnetic field, i.e., on the O^H site [62]. In regards to the charge distribution, $\sim$90 % of HS-Mn^{3+}: $t_{2g}^3 \uparrow e_g^1 \uparrow$ and 10 % of HS-Mn^{2+}: $t_{2g}^3 \uparrow e_g^2 \uparrow$ can be estimated from the K- and $L_{2,3}$-edge XANES, resulting in a overall charge of 2.9+ $\pm$ 0.3. The slightly increased inaccuracy in the oxidation state, compared to other cations, might originate from a minor fraction of charge disproportionation [68,69], where O^H HS-Mn^{4+} and additional O^H HS-Mn^{2+} form at the expense of O^H HS-Mn^{3+}.

The line shapes and the peak position in the Ni $L_{2,3}$ XANES spectrum (Figure 5d) are similar to those for the Ni^{2+} state, which supplement the information obtained from the K-edge XANES [70]. The XMCD fine structure along with intense negative p at 853.4 eV corresponding to the L_3 edge and the positive m_{tot} as a consequence (Supplementary Table SI2) indicate the presence of Ni^{2+} in the HS O^H environment, i.e., $3d^8$: $t_{2g}^6 e_g^2 \uparrow$ [70]. The experimental XANES and XMCD spectra and values obtained from sum rules are in good agreement with the multiplet calculations fit, as presented in Supplementary Figure SI6e and Table SI3.

Thus, the $L_{2,3}$-edge XANES and XMCD along with the multiplet calculations, K-edge XANES, and ^{57}Fe Mössbauer spectroscopy provide a near complete model of the occupations and spin-electronic structure of the S-HEO. The overall average oxidation state of the cations is close 2.66+, as summarized in Table 2. This further supports the crystallization of the studied composition into a 1:2:4 oxide spinel structure. In addition, the element specific magnetic moments and the spin-orientations are also precisely estimated from the $L_{2,3}$-edge XANES and XMCD. The overall magnetic moment obtained from the experimental sum rule analysis is less than 15 % off compared to the bulk magnetic moment obtained from spatially averaging SQUID magnetometry, while the agreement between the bulk moment and the overall moment obtained from multiplet calculations is even better (Table 2). This correlation further strengthens the obtained ionic distribution model. Given this knowledge, NPD is used as the final complementary step to derive the complete crystallographic and magnetic structure of the S-HEO.

Table 2
The oxidation states (Ox.), spin-electronic states, average oxidation states (Avg. Ox.) and occupation of the different cations per formula unit (f.u.) of the S-HEO, $(Co_{0.2}Cr_{0.2}Fe_{0.2}Mn_{0.2}Ni_{0.2})_3O_4$, obtained from the combination of spectroscopic and diffraction approach are summarized. It should be noted that the spin states are presented with respect to the magnetization and the applied field. As Fe^{3+} occupies both sites, the effective spin-state is provided. The effective magnetic moments at 5 K per f.u. obtained from SQUID magnetometry (m_{eff}, SQUID), XMCD sum rules (m_{eff}, XMCD), multiplet calculations (m_{eff}, MC) and neutron diffraction (m_{eff}, NPD) are presented.

Elements	Ox.	Spin-state	T^D	O^H	Avg. Ox.
Co	2	$e^4 t_2^3 \downarrow$	0.36	-	2.4(2)
	3	$e^2 \downarrow e^1 \uparrow t_2^3 \downarrow$	0.24	-	
Cr	3	$t_{2g}^3 \uparrow$	-	0.6	3.0(0)
Fe	3	$e^2 \downarrow t_2^3 \downarrow$	0.4	0.2	3.0(0)
Mn	3	$t_{2g}^3 \uparrow e_g^1 \uparrow$	-	0.54	2.9(3)
	2	$t_{2g}^3 \uparrow e_g^2 \uparrow$	-	0.06	
Ni	2	$t_{2g}^6 e_g^2 \uparrow$	-	0.6	2.0(0)
m_{eff}, SQUID					1.7(1) μ_B/f.u.
m_{eff}, XMCD					1.5(4) μ_B/f.u.
m_{eff}, MC					1.7(1) μ_B/f.u.
m_{eff}, NPD					1.5(2) μ_B/f.u.

3.6. Complete structural and magnetic model: Neutron powder diffraction

NPD is used as the final characterization tool for validation of the observed cationic distribution. The neutron scattering length of the constituent elements (in barn) are as follows: 2.49 for Co, 3.64 for Cr, 9.45 for Fe, -3.73 for Mn, 10.3 for Ni and 5.80 for O. Although neutrons provide the capability to distinguish between the cations and estimate the presence of oxygen vacancies, a fully unconstrained structural refinement is still not feasible as the scattering powers of Fe and Ni are too similar. Nevertheless, the combination of NPD with the results from K and $L_{2,3}$ XANES and XMCD affords a great precision by overcoming the limitations of the individual techniques. Out of the several models tried that are close to the predictions made from XANES and XMCD, the best goodness of fit was obtained when Co was placed solely in T^D while the rest of T^D was populated by Fe. Placing some of the Co on the O^H site, mimicking possible LS-Co^{3+}, something difficult to judge from XMCD, while the remaining T^D is occupied by Fe or Mn leads to a poorer fit of the results. Thus, the combination of these results obtained from several complementary techniques, allows for estimating structural model with great precision (i.e., occupation of cations) of the S-HEO, which is very close to $(Co_{0.6}Fe_{0.4})(Cr_{0.3}Fe_{0.1}Mn_{0.3}Ni_{0.3})_2O_4$. Using the structural model, the occupation of oxygen in 32e was also refined. Negligible variation in the oxygen occupation from NPD indicate stoichiometric oxygen content in S-HEO, which further supports the fact that the overall average cation charge in the system is close to 2.66+ (Table 2). The obtained structural model with the oxidation states is expected to be close to $(Co_{0.6}^{2.4+}Fe_{0.4}^{3+})(Cr_{0.3}^{3+}Fe_{0.1}^{3+}Mn_{0.3}^{2.9+}Ni_{0.3}^{2+})_2O_4$ (Figure 6). However, as earlier discussed minor inaccuracies $\sim$10 % in the overall oxidation state of Co and Mn, resulting in a charge compensation between these two cations, remain a possibility where slightly more Co^{2+} and correspondingly a fraction of Mn^{4+} at the expense of Mn^{3+} is possible. In addition to the nuclear scattering, we need to consider the existing magnetic structure, especially in order to refine the intensities of high d-spacing reflections correctly. No additional reflections apart from the ones allowed by a symmetry of $Fd\bar{3}m$ (227) could be observed in Figure 6a, indicating the crystallographic commensurate ferrimagnetic structure of S-HEO, i.e., $k = [000]$. Table 2 provides an overview of the results obtained from the combination of the different spectroscopic and diffraction techniques used in this study. The expected magnetic moment from NPD (Table 2), further complements the obtained

Table 3

The configuration entropy per mole of atom ($\frac{S_{config}}{atom}$), per mole of formula unit ($\frac{S_{config}}{f.u.}$) and per mole of cation ($\frac{S_{config}}{cation}$) for the different occupational models mentioned in Figure 6c are tabulated here. In addition, the S_{config} for rocksalt-HEO (R-HEO) is included for comparison, where the relationships between $\frac{S_{config}}{atom}$, $\frac{S_{config}}{f.u.}$ and $\frac{S_{config}}{cation}$ are different compared to the spinels. It should be noted that in all cases stoichiometric oxygen content has been assumed, while for the observed scenario, i.e., $(Co_{0.6}Fe_{0.4})(Cr_{0.3}Fe_{0.1}Mn_{0.3}Ni_{0.3})_2O_4$, it has been experimentally validated. R is the universal gas constant.

Composition	Short name	$\frac{S_{config}}{atom}$	$\frac{S_{config}}{f.u.}$	$\frac{S_{config}}{cation}$
$(Co_{0.2}Cr_{0.2}Fe_{0.2}Mn_{0.2}Ni_{0.2})(Co_{0.2}Cr_{0.2}Fe_{0.2}Mn_{0.2}Ni_{0.2})_2O_4$	Disordered	0.69 R	4.83 R	1.61 R
$(Co_{0.05}Cr_{0.35}Fe_{0.35}Mn_{0.05}Ni_{0.2})(Co_{0.275}Cr_{0.125}Fe_{0.125}Mn_{0.275}Ni_{0.2})_2O_4$	KKR-CPA [30]	0.64 R	4.48 R	1.49 R
$(Co_{0.36}Cr_{0.06}Ni_{0.06})(Co_{0.12}Cr_{0.3}Fe_{0.3}Mn_{0.3})_2O_4$	Normal	0.500 R	3.50 R	1.17 R
$(Co_{0.34}Mn_{0.06}Fe_{0.6})(Co_{0.13}Cr_{0.3}Mn_{0.27}Ni_{0.3})_2O_4$	CFSE-favored	0.504 R	3.52 R	1.18 R
$(Co_{0.6}Fe_{0.4})(Cr_{0.3}Fe_{0.1}Mn_{0.3}Ni_{0.3})_2O_4$	Observed	0.47 R	3.30 R	1.10 R
$(Co_{0.2}Cu_{0.2}Mg_{0.2}Ni_{0.2}Zn_{0.2})O$	R-HEO [2,3]	0.80 R	1.61 R	1.61 R

structural model: $(Co_{0.6}Fe_{0.4})(Cr_{0.3}Fe_{0.1}Mn_{0.3}Ni_{0.3})_2O_4$ (as shown in Figure 6b).

4. Discussion

Cation occupation in oxide spinels is largely dictated by two governing factors: one is the crystal field stabilization energy (CFSE) in the oxygen ligand field, while the other one is the configuration entropy (S_{config}) gain arising from the disordered arrangement due to anti-site mixing. The ideal S_{config} per mole of atom in a system, especially with multiple sub-lattices, can be calculated using the sub-lattice model ([16,71–74]) as presented in Equation 1:

$$\frac{S_{config}}{atom} = -R\left(\frac{\sum_{x=1}^{x} a^x \sum_{N=1}^{N}(f_i^x ln f_i^x)}{\sum_{x=1}^{x} a^x}\right) \tag{1}$$

where, R is the universal gas constant, a^x is the number of sites on the x sub-lattice, f_i^x is the fraction of elemental species randomly distributed on the respective sub-lattice and N is the number of elements in a given sub-lattice.

For 1:2:4 oxide spinel, the Equation 1 can be written as follows:

$$\frac{S_{config}}{atom} = \frac{R}{7}[1*\sum_{P=1}^{P}(f_p ln f_p)_{T^D} + 2*\sum_{Q=1}^{Q}(f_q ln f_q)_{O^H} + 4*\sum_{O=1}^{O}(f_o ln f_o)_O] \tag{2}$$

where total number of atoms per formula unit is $\sum_{x=1}^{x} a^x = 7$, P, Q, O refer to the number of elements on the different sub-lattices, T^D, O^H and oxygen (anion), respectively, while f_p, f_q, f_o refer to the atomic fractions of the elements on the respective sub-lattices. For instance, in case of $(Co_{0.6}Fe_{0.4})(Cr_{0.3}Fe_{0.1}Mn_{0.3}Ni_{0.3})_2O_4$, the $\frac{S_{config}}{atom}$ can be defined as follows:

$$\frac{S_{config}}{atom} = \frac{R}{7}[1*(0.6ln0.6+0.4ln0.4) + 2*(0.3ln0.3+0.1ln0.1+0.3ln0.3+0.3ln0.3) + 4*(1ln1))] \tag{3}$$

As can be observed, the factor $ln f_o = 0$ due to the stoichiometric oxygen content. In addition, the configuration entropy per mole of formula unit $\frac{S_{config}}{f.u.}$ and configuration entropy per mole of cation $\frac{S_{config}}{cation}$ in 1:2:4 spinel can calculated as follows:

$$\frac{S_{config}}{f.u.} = 7*\frac{S_{config}}{atom} \tag{4}$$

$$\frac{S_{config}}{cation} = \frac{7}{3}*\frac{S_{config}}{atom} \tag{5}$$

Table 3 compares the S_{config} values for the cation occupation model obtained from this study, with some of the extreme occupational scenarios and the model obtained from the KKR-CPA study[30]. The $\frac{S_{config}}{cation}$ can be considered as a more reliable metric to compare the S_{config} among HEOs, consisting multiple cations on

different cation sub-lattices. Figure 6c schematically compares the $\frac{S_{config}}{cation}$ and CFSE for these different cationic occupations possible in the studied S-HEO. The details of the calculation for CFSE for the different occupation models are provided in Supplementary Table SI4-9.

The $\frac{S_{config}}{cation}$ with a complete "disorder" (i.e., equal distribution of cations in O^H and T^D site) is equal to 1.61 R, similar to that of a five cation rocksalt-HEO. This value is considerably higher than the "observed" scenario (Figure 6c) with $\frac{S_{config}}{cation} = 1.10$ R. The deviation from the highest disordered state can be explained using the CFSE or the octahedral site preferential energy/enthalpy (OSPE) for a particular cation (Supplementary Table SI5). It is clear that CFSE/OSPE plays a dominant role over configurational disorder in determining the occupation of the cations. However, as Figure 6c and Supplementary Table SI5 indicate, CFSE/OSPE is not the sole player, otherwise $3d^5$ Fe^{3+} and Mn^{2+}, especially Mn^{2+} with comparatively larger cationic radii in a six-fold coordination, should be preferred on the T^D over HS Co^{2+}/Co^{3+}. In fact, the enthalpy favorable structural model ("CFSE favored", Figure 6c), $(Co_{0.34}Fe_{0.3}Mn_{0.06})(Co_{0.13}Cr_{0.3}Mn_{0.27}Ni_{0.3})_2O_4$, should ideally result in higher S_{config} of 1.18 R. This certainly indicates a role of other competing thermodynamic features influencing the cation occupancy, exploration of which remains a subject for future endeavor. A possible influence of temperature, pressure and size/surface effects on the cationic distribution and anti-site mixing will be worth exploring in the future. This is because even in the case of conventional spinel systems, it is known that the cationic distribution can vary because of these aforementioned factors [47,75]. Endeavors in this direction will not only help to better understand the nature of cationic ordering in S-HEO as a function of temperature and/or pressure but can also be useful to predict their temperature/pressure dependent functional properties.

The ionic ordering due to the enthalpy factors (CFSE) observed in the S-HEO here is inherently correlated to the magnetic properties. As observed, the S-HEO exhibits a Néel type ferrimagnetic ground state, which means the magnetism is governed by the intersite AFM coupling. This means that any change in the cation occupation will have a direct impact on the overall ferrimagentic moment, which is verified by utilizing multiple techniques used in this study (Table 2). Likewise, depending upon the cation distribution over the respective sites different magnetic ground states and transition temperatures can also be expected. In fact, the presence of cation order can also be anticipated in other HEO-classes, which can have a decisive impact on their functional properties. A few scenarios that can be of immediate interest for future explorations are considered here. Perovskite-HEOs exhibit a magnetic phase separation that manifests itself through a vertical exchange bias [8]. It is assumed that ferromagnetic clusters are present within the predominant antiferromagnetic lattice, which can perhaps be an indication of chemical short-range ordering of cations that couple ferromagnetically via the bridging oxygen. Likewise, even in the

case of rocksalt-HEOs [9,39], the anomalous heat capacity behavior around the Néel temperature hints towards short range magnetic correlations well above the Néel temperature that can also be an outcome of a certain degree of local chemical ordering. In addition, the extent of cation order can also play a major role in the energy storage capabilities in the case of layered-HEOs [76,77]. For instance, in the case of conventional layered Li-delafossites an ordered Li sub-lattice is preferred for better performance [78]. Hence, the extent of cation ordering on a lattice level, as observed here, or chemical short-range ordering leading to local lowering of crystallographic symmetry can be extremely crucial for better understanding the unique properties exhibited by the HEOs, which warrants future studies along this direction.

5. Conclusions

This demonstration study focusses on a multi-functional spinel-HEO, $(Co_{0.2}Cr_{0.2}Fe_{0.2}Mn_{0.2}Ni_{0.2})_3O_4$. To overcome the experimental limitations, stemming from the presence of multiple principal cations with different occupation and spin-electronic states, we devised and followed a cross-referenced experimental approach to determine the crystallographic, magnetic and spin-electronic structure of the spinel-HEO. X-ray magnetic circular dichroism (XMCD) along with X-Ray absorption spectroscopy (XANES) at the transition metal L-edges was used as the primary technique to unravel the cationic occupation along with the element specific magnetic behavior. TM K-edge XANES, ^{57}Fe Mössbauer spectroscopy (in presence and absence of magnetic field), neutron diffraction and SQUID magnetometery have been further utilized to complement the obtained results. An $Fd\bar{3}m$ structure with Néel-type collinear ferrimagnetic spin arrangement and elemental distribution model close to $(Co_{0.6}Fe_{0.4})(Cr_{0.3}Fe_{0.1}Mn_{0.3}Ni_{0.3})_2O_4$ is observed. In contrast to the existing reports on the spinel-HEO, the observed structural model reveals significant preferences in cationic occupation resulting in the lowest configuration entropy allowed by the given composition in a spinel structure. The observed structure indicates the crucial role of the fundamental enthalpy factors, such as CFSE, in governing the cations occupancy in the spinel-HEO. On a practical level, the detailed structural and magnetic mapping can help to build a knowledge-sharing platform for elucidation and prediction of the properties in the multifunctional spinel-HEO that are governed by the cationic distribution. In the broader context, this initial study highlights significant deviation from a completely disordered configuration often assumed in HEOs, prompting the necessity of comprehensive and complementary studies to determine the actual contribution of configurational entropy. A precise determination of the actual degree of chemical ordering from a lattice perspective or even short-range chemical ordering, resulting in local lowering of crystallographic symmetry, can potentially open up further opportunities for property tailoring in HEOs.

Declaration of Competing Interest

The authors declare that they have no known competing financial interests or personal relationships that could have appeared to influence the work reported in this paper.

Acknowledgments

Supplementary material

Supplementary material associated with this article can be found, in the online version, at doi:10.1016/j.actamat.2021.117581

References

[1] B. Cantor, I. Chang, P. Knight, A. Vincent, Microstructural development in equiatomic multicomponent alloys, Materials Science and Engineering: A 375-377 (2004) 213–218, doi:10.1016/j.msea.2003.10.257. https://linkinghub.elsevier.com/retrieve/pii/S0921509303009936

[2] C.M. Rost, E. Sachet, T. Borman, A. Moballegh, E.C. Dickey, D. Hou, J.L. Jones, S. Curtarolo, J.-P. Maria, Entropy-stabilized oxides, Nature Communications 6 (1) (2015) 8485, doi:10.1038/ncomms9485. http://www.nature.com/articles/ncomms9485

[3] D. Bérardan, S. Franger, A.K. Meena, N. Dragoe, Room temperature lithium superionic conductivity in high entropy oxides, Journal of Materials Chemistry A 4 (24) (2016) 9536–9541, doi:10.1039/C6TA03249D. http://xlink.rsc.org/?DOI=C6TA03249D

[4] A. Sarkar, L. Velasco, D. Wang, Q. Wang, G. Talasila, L. de Biasi, C. Kübel, T. Brezesinski, S.S. Bhattacharya, H. Hahn, B. Breitung, High entropy oxides for reversible energy storage, Nature Communications 9 (1) (2018) 3400, doi:10.1038/s41467-018-05774-5. http://www.nature.com/articles/s41467-018-05774-5

[5] C. Oses, C. Toher, S. Curtarolo, High-entropy ceramics, Nature Reviews Materials (2020), doi:10.1038/s41578-019-0170-8. http://www.nature.com/articles/s41578-019-0170-8

[6] G. Anand, A.P. Wynn, C.M. Handley, C.L. Freeman, Phase stability and distortion in high-entropy oxides, Acta Materialia 146 (2018) 119–125, doi:10.1016/j.actamat.2017.12.037. https://www.sciencedirect.com/science/article/abs/pii/S1359645417310492

[7] A. Sarkar, Q. Wang, A. Schiele, M.R. Chellali, S.S. Bhattacharya, D. Wang, T. Brezesinski, H. Hahn, L. Velasco, B. Breitung, High-Entropy Oxides: Fundamental Aspects and Electrochemical Properties, Advanced Materials 31 (26) (2019) 1806236, doi:10.1002/adma.201806236. https://onlinelibrary.wiley.com/doi/abs/10.1002/adma.201806236

[8] R. Witte, A. Sarkar, R. Kruk, B. Eggert, R.A. Brand, H. Wende, H. Hahn, High-entropy oxides: An emerging prospect for magnetic rare-earth transition metal perovskites, Physical Review Materials 3 (3) (2019) 034406, doi:10.1103/PhysRevMaterials.3.034406. 10.1103/PhysRevMaterials.3.034406

[9] J. Zhang, J. Yan, S. Calder, Q. Zheng, M.A. McGuire, D.L. Abernathy, Y. Ren, S.H. Lapidus, K. Page, H. Zheng, J.W. Freeland, J.D. Budai, R.P. Hermann, Long-Range Antiferromagnetic Order in a Rocksalt High Entropy Oxide, Chem. Mater. 31 (10) (2019) 3705, doi:10.1021/acs.chemmater.9b00624. https://pubs.acs.org/sharingguidelines

[10] H. Xu, Z. Zhang, J. Liu, C.-L. Do-Thanh, H. Chen, S. Xu, Q. Lin, Y. Jiao, J. Wang, Y. Wang, Y. Chen, S. Dai, Entropy-stabilized single-atom Pd catalysts via high-entropy fluorite oxide supports, Nature Communications 11 (1) (2020) 1–9, doi:10.1038/s41467-020-17738-9.

[11] Q. Wang, A. Sarkar, D. Wang, L. Velasco, R. Azmi, S.S. Bhattacharya, T. Bergfeldt, A. Düvel, P. Heitjans, T. Brezesinski, H. Hahn, B. Breitung, Multi-anionic and -cationic compounds: new high entropy materials for advanced Li-ion batteries, Energy Environ. Sci. 12 (8) (2019) 2433–2442, doi:10.1039/C9EE00368A. http://xlink.rsc.org/?DOI=C9EE00368A

[12] Z. Lun, B. Ouyang, D.-H. Kwon, Y. Ha, E.E. Foley, T.-Y. Huang, Z. Cai, H. Kim, M. Balasubramanian, Y. Sun, J. Huang, Y. Tian, H. Kim, B.D. McCloskey, W. Yang, R.J. Clément, H. Ji, G. Ceder, Cation-disordered rocksalt-type high-entropy cathodes for Li-ion batteries, Nature Materials 20 (2) (2021) 214–221, doi:10.1038/s41563-020-00816-0. http://www.nature.com/articles/s41563-020-00816-0

[13] Y. Sharma, Q. Zheng, A.R. Mazza, E. Skoropata, T. Heitmann, Z. Gai, B. Musico, P.F. Miceli, B.C. Sales, V. Keppens, M. Brahlek, T.Z. Ward, Magnetic anisotropy in single-crystal high-entropy perovskite oxide La(Cr_{0.2}Mn_{0.2}Fe_{0.2}Co_{0.2}Ni_{0.2})o_3 films, Phys. Rev. Materials 4 (2020) 014404, doi:10.1103/PhysRevMaterials.4.014404. https://link.aps.org/doi/10.1103/PhysRevMaterials.4.014404

[14] Q. Ding, Y. Zhang, X. Chen, X. Fu, D. Chen, S. Chen, L. Gu, F. Wei, H. Bei, Y. Gao, M. Wen, J. Li, Z. Zhang, T. Zhu, R.O. Ritchie, Q. Yu, Tuning element distribution, structure and properties by composition in high-entropy alloys, Nature 574 (7777) (2019) 223–227, doi:10.1038/s41586-019-1617-1.

[15] R. Zhang, S. Zhao, J. Ding, Y. Chong, T. Jia, C. Ophus, M. Asta, R.O. Ritchie, A.M. Minor, Short-range order and its impact on the crconi medium-entropy alloy, Nature 581 (7808) (2020) 283–287, doi:10.1038/s41586-020-2275-z.

[16] A. Navrotsky, O.J. Kleppa, The thermodynamics of cation distributions in simple spinels, Journal of Inorganic and Nuclear Chemistry 29 (11) (1967) 2701–2714, doi:10.1016/0022-1902(67)80008-3. https://www.sciencedirect.com/science/article/pii/0022190267800083

[17] J. Dąbrowa, M. Stygar, A. Mikuła, A. Knapik, K. Mroczka, W. Tejchman, M. Danielewski, M. Martin, Synthesis and microstructure of the

(Co,Cr,Fe,Mn,Ni)3O4high entropy oxide characterized by spinel structure, Mater. Lett. 216 (2018) 32–36, doi:10.1016/j.matlet.2017.12.148.

[18] S.H. Albedwawi, A. AlJaberi, G.N. Haidemenopoulos, K. Polychronopoulou, High entropy oxides-exploring a paradigm of promising catalysts: A review, Materials & Design 202 (2021) 109534, doi:10.1016/j.matdes.2021.109534. https://www.sciencedirect.com/science/article/pii/S0264127521000873

[19] A. Salian, S. Mandal, Entropy stabilized multicomponent oxides with diverse functionality - a review, Critical Reviews in Solid State and Materials Sciences 0 (0) (2021) 1–52, doi:10.1080/10408436.2021.1886047.

[20] M. Fracchia, M. Manzoli, U. Anselmi-Tamburini, P. Ghigna, A new eight-cation inverse high entropy spinel with large configurational entropy in both tetrahedral and octahedral sites: Synthesis and cation distribution by X-ray absorption spectroscopy, Scripta Materialia 188 (2020) 26–31, doi:10.1016/j.scriptamat.2020.07.002. http://www.sciencedirect.com/science/article/pii/S1359646220304413

[21] A. Mao, H.-Z. Xiang, Z.-G. Zhang, K. Kuramoto, H. Zhang, Y. Jia, A new class of spinel high-entropy oxides with controllable magnetic properties, Journal of Magnetism and Magnetic Materials 497 (2020) 165884, doi:10.1016/j.jmmm.2019.165884. https://linkinghub.elsevier.com/retrieve/pii/S0304885319325740

[22] B. Musicó, Q. Wright, T.Z. Ward, A. Grutter, E. Arenholz, D. Gilbert, D. Mandrus, V. Keppens, Tunable magnetic ordering through cation selection in entropic spinel oxides, Physical Review Materials 3 (10) (2019) 104416, doi:10.1103/PhysRevMaterials.3.104416. https://link.aps.org/doi/10.1103/PhysRevMaterials.3.104416

[23] D. Wang, S. Jiang, C. Duan, J. Mao, Y. Dong, K. Dong, Z. Wang, S. Luo, Y. Liu, X. Qi, Spinel-structured high entropy oxide (FeCoNiCrMn)3O4 as anode towards superior lithium storage performance, Journal of Alloys and Compounds 844 (2020) 156158, doi:10.1016/j.jallcom.2020.156158. http://www.sciencedirect.com/science/article/pii/S0925838820325226

[24] T.X. Nguyen, J. Patra, J.-K. Chang, J.-M. Ting, High entropy spinel oxide nanoparticles for superior lithiation-delithiation performance, 2020, doi:10.1039/D0TA04844E. https://doi.org/10.1039/D0TA04844E

[25] C.-C. Lin, C.-W. Chang, C.-C. Kaun, Y.-H. Su, Stepwise evolution of photocatalytic spinel-structured (co,cr,fe,mn,ni)3o4 high entropy oxides from first-principles calculations to machine learning, Crystals 11 (9) (2021), doi:10.3390/cryst11091035. https://www.mdpi.com/2073-4352/11/9/1035

[26] T.X. Nguyen, Y.-H. Su, J. Hattrick-Simpers, H. Joress, T. Nagata, K.-S. Chang, S. Sarker, A. Mehta, J.-M. Ting, Exploring the first high-entropy thin film libraries: Composition spread-controlled crystalline structure, ACS Combinatorial Science 22 (12) (2020) 858–866, doi:10.1021/acscombsci.0c00159. PMID: 33146510

[27] B. Talluri, M. Aparna, N. Sreenivasulu, S. Bhattacharya, T. Thomas, High entropy spinel metal oxide (cocrfemnni)3o4 nanoparticles as a high-performance supercapacitor electrode material, Journal of Energy Storage 42 (2021) 103004, doi:10.1016/j.est.2021.103004. https://www.sciencedirect.com/science/article/pii/S2352152X21007180

[28] C.-Y. Huang, C.-W. Huang, M.-C. Wu, J. Patra, T. Xuyen Nguyen, M.-T. Chang, O. Clemens, J.-M. Ting, J. Li, J.-K. Chang, W.-W. Wu, Atomic-scale investigation of lithiation/delithiation mechanism in high-entropy spinel oxide with superior electrochemical performance, Chemical Engineering Journal 420 (2021) 129838, doi:10.1016/j.cej.2021.129838. https://www.sciencedirect.com/science/article/pii/S1385894721014236

[29] A. Mao, F. Quan, H.-Z. Xiang, Z.-G. Zhang, K. Kuramoto, A.-L. Xia, Facile synthesis and ferrimagnetic property of spinel (cocrfemnni)3o4 high-entropy oxide nanocrystalline powder, Journal of Molecular Structure 1194 (2019) 11–18, doi:10.1016/j.molstruc.2019.05.073. https://www.sciencedirect.com/science/article/pii/S002228601930643X

[30] J. Cieslak, M. Reissner, K. Berent, J. Dabrowa, M. Stygar, M. Mozdzierz, M. Zajusz, Magnetic properties and ionic distribution in high entropy spinels studied by Mössbauer and ab initio methods, Acta Materialia 206 (2021) 116600, doi:10.1016/j.actamat.2020.116600. http://www.sciencedirect.com/science/article/pii/S1359645420310375

[31] Z. Grzesik, G. Smoła, M. Miszczak, M. Stygar, J. Däbrowa, M. Zajusz, K. Świerczek, M. Danielewski, Defect structure and transport properties of (co,cr,fe,mn,ni)3o4 spinel-structured high entropy oxide, Journal of the European Ceramic Society 40 (3) (2020) 835–839, doi:10.1016/j.jeurceramsoc.2019.10.026. https://www.sciencedirect.com/science/article/pii/S0955221919306971

[32] T.X. Nguyen, Y.-H. Su, C.-C. Lin, J. Ruan, J.-M. Ting, A new high entropy glycerate for high performance oxygen evolution reaction, Advanced Science 8 (6) (2021) 2002446, doi:10.1002/advs.202002446.

[33] M. Stygar, J. Däbrowa, M. Modzierz, M. Zajusz, W. Skubida, K. Mroczka, K. Berent, K. Świerczek, M. Danielewski, Formation and properties of high entropy oxides in co-cr-fe-mg-mn-ni-o system: Novel (cr,fe,mg,mn,ni)3o4 and (co,cr,fe,mg,mn)3o4 high entropy spinels, Journal of the European Ceramic Society 40 (4) (2020) 1644–1650, doi:10.1016/j.jeurceramsoc.2019.11.030. https://www.sciencedirect.com/science/article/pii/S0955221919307757

[34] Topas V5, General profile and structure analysis software for powder diffraction data, User's Manual, Bruker AXS, Karlsruhe.

[35] E. Welter, R. Chernikov, M. Herrmann, R. Nemausat, A beamline for bulk sample x-ray absorption spectroscopy at the high brilliance storage ring PETRA III, AIP Conference Proceedings 2054 (2019) 2–6, doi:10.1063/1.5084603.

[36] E. Weschke, E. Schierle, The UE46 PGM-1 beamline at BESSY II, Journal of large-scale research facilities JLSRF 4 (2018) 1–12, doi:10.17815/jlsrf-4-77.

[37] M. Retegan, Crispy: v0.7.3, 2019, (????). 10.5281/zenodo.1008184.

[38] E. Stavitski, F.M. de Groot, The CTM4xas program for EELS and XAS spectral shape analysis of transition metal l edges, Micron 41 (7) (2010) 687–694, doi:10.1016/j.micron.2010.06.005.

[39] Z. Rák, D.W. Brenner, Exchange interactions and long-range magnetic order in the (mg,co,cu,ni,zn)o entropy-stabilized oxide: A theoretical investigation, Journal of Applied Physics 127 (18) (2020) 185108, doi:10.1063/5.0008258.

[40] Ç.E. Demirci, P.K. Manna, Y. Wroczynskyj, S. Aktürk, J. van Lierop, A comparison of the magnetism of cobalt-, manganese-, and nickel-ferrite nanoparticles, Journal of Physics D: Applied Physics 51 (2) (2017) 25003, doi:10.1088/1361-6463/aa9d79.

[41] O. Clemens, M. Gröting, R. Witte, J.M. Perez-Mato, C. Loho, F.J. Berry, R. Kruk, K.S. Knight, A.J. Wright, H. Hahn, P.R. Slater, Crystallographic and magnetic structure of the perovskite-type compound bafeo2.5: Unrivaled complexity in oxygen vacancy ordering, Inorganic Chemistry 53 (12) (2014) 5911–5921, doi:10.1021/ic402988y.

[42] J. Chappert, R.B. Frankel, Mössbauer study of ferrimagnetic ordering in nickel ferrite and chromium-substituted nickel ferrite, Phys. Rev. Lett. 19 (1967) 570–572, doi:10.1103/PhysRevLett.19.570.

[43] F. de Groot, High-resolution x-ray emission and x-ray absorption spectroscopy, Chemical Reviews 101 (6) (2001) 1779–1808, doi:10.1021/cr9900681.

[44] F. de Groot, G. Vankó, P. Glatzel, The 1s x-ray absorption pre-edge structures in transition metal oxides, Journal of Physics: Condensed Matter 21 (10) (2009) 104207, doi:10.1088/0953-8984/21/10/104207.

[45] M. Hunault, G. Calas, L. Galoisy, G. Lelong, M. Newville, Local Ordering Around Tetrahedral Co2+ in Silicate Glasses, Journal of the American Ceramic Society 97 (1) (2014) 60–62, doi:10.1111/jace.12709.

[46] A. Moen, D.G. Nicholson, M. Rnning, G.M. Lamble, J.-F. Lee, H. Emerich, X-Ray absorption spectroscopic study at the cobalt K-edge on the calcination and reduction of the microporous cobalt silicoaluminophosphate catalyst CoSAPO-34, Journal of the Chemical Society, Faraday Transactions 93 (22) (1997) 4071–4077, doi:10.1039/a704488g.

[47] S. Chen, Y. Wu, P. Cui, W. Chu, X. Chen, Z. Wu, Cation distribution in zncr2o4 nanocrystals investigated by x-ray absorption fine structure spectroscopy, The Journal of Physical Chemistry C 117 (47) (2013) 25019–25025, doi:10.1021/jp404984y.

[48] K.E. Miyano, J.C. Woicik, P. Sujatha Devi, H.D. Gafney, Cr K edge x-ray absorption study of Cr dopants in Mg2SiO4 and Ca2GeO4, Applied Physics Letters 71 (9) (1997) 1168–1170, doi:10.1063/1.119615.

[49] J. Dubrail, F. Farges, Not all chromates show the same pre-edge feature. implications for the modelling of the speciation of cr in environmental systems, Journal of Physics: Conference Series 190 (2009) 012176, doi:10.1088/1742-6596/190/1/012176.

[50] P. Zimmermann, N. Bouldi, M.O. Hunault, M. Sikora, J.M. Ablett, J.-P. Rueff, B. Lebert, P. Sainctavit, F.M. de Groot, A. Juhin, 1s2p resonant inelastic x-ray scattering magnetic circular dichroism as a probe for the local and non-local orbitals in cro2, Journal of Electron Spectroscopy and Related Phenomena 222 (2018) 74–87, doi:10.1016/j.elspec.2017.08.004. https://www.sciencedirect.com/science/article/pii/S0368204816301682

[51] D. Carta, G. Mountjoy, G. Navarra, M.F. Casula, D. Loche, S. Marras, A. Corrias, X-ray absorption investigation of the formation of cobalt ferrite nanoparticles in an aerogel silica matrix, The Journal of Physical Chemistry C 111 (17) (2007) 6308–6317, doi:10.1021/jp0708805.

[52] D. Carta, D. Loche, G. Mountjoy, G. Navarra, A. Corrias, Nife2o4 nanoparticles dispersed in an aerogel silica matrix: An x-ray absorption study, The Journal of Physical Chemistry C 112 (40) (2008) 15623–15630, doi:10.1021/jp803982k.

[53] E. Chalmin, F. Farges, G.E. Brown, A pre-edge analysis of mn k-edge xanes spectra to help determine the speciation of manganese in minerals and glasses, Contributions to Mineralogy and Petrology 157 (1) (2009) 111–126, doi:10.1007/s00410-008-0323-z.

[54] F. Liu, W. Shan, Z. Lian, L. Xie, W. Yang, H. He, Novel MnWOx catalyst with remarkable performance for low temperature NH3-SCR of NOx, Catal. Sci. Technol. 3 (10) (2013) 2699–2707, doi:10.1039/C3CY00326D.

[55] A. Anspoks, A. Kuzmin, Interpretation of the Ni K-edge EXAFS in nanocrystalline nickel oxide using molecular dynamics simulations, Journal of Non-Crystalline Solids 357 (14) (2011) 2604–2610, doi:10.1016/j.jnoncrysol.2011.02.030. http://www.sciencedirect.com/science/article/pii/S0022309311001724

[56] C.T. Chen, Y.U. Idzerda, H.-J. Lin, N.V. Smith, G. Meigs, E. Chaban, G.H. Ho, E. Pellegrin, F. Sette, Experimental Confirmation of the X-Ray Magnetic Circular Dichroism Sum Rules for Iron and Cobalt, Physical Review Letters 75 (1) (1995) 152–155, doi:10.1103/PhysRevLett.75.152. https://journals.aps.org/prl/pdf/10.1103/PhysRevLett.75.152

[57] P. Carra, B.T. Thole, M. Altarelli, X. Wang, X-Ray Circular Dichroism and Local Magnetic Fields, Phys. Rev. Lett. 70 (1993) 694. https://journals.aps.org/prl/pdf/10.1103/PhysRevLett.70.694

[58] H. Wende, C. Antoniak, Magnetism and Synchrotron Radiation, Springer, Berlin, Heidelberg, 2010, pp. 145–167.

[59] C. Piamonteze, P. Miedema, F.M.F. de Groot, Accuracy of the spin sum rule in xmcd for the transition-metal l edges from manganese to copper, Phys. Rev. B 80 (2009) 184410, doi:10.1103/PhysRevB.80.184410.

[60] S. Yang, C. Feng, D. Spence, A.M.A.A. Al Hindawi, E. Latimer, A.M. Ellis, C. Binns, D. Peddis, S.S. Dhesi, L. Zhang, Y. Zhang, K.N. Trohidou, M. Vasilakaki, N. Ntallis, I. MacLaren, F.M.F. de Groot, Robust ferromagnetism of chromium nanoparticles formed in superfluid helium, Advanced Materials 29 (1) (2017) 1604277, doi:10.1002/adma.201604277. https://onlinelibrary.wiley.com/doi/abs/10.1002/adma.201604277

[61] M.Y. Yang, S. Seong, E. Lee, M. Ghanathe, A. Kumar, S.M. Yusuf, Y. Kim, J.-S. Kang, Electronic structures and magnetization reversal in Li 0.5 FeCr 1.5 O 4, Applied Physics Letters 116 (25) (2020) 252401, doi:10.1063/5.0007411. http://aip.scitation.org/doi/10.1063/5.0007411.

[62] J. Garcia-Barriocanal, J. Cezar, F.Y. Bruno, P. Thakur, N. Brookes, C. Utfeld, A. Rivera-Calzada, S. Giblin, J. Taylor, J. Duffy, et al., Spin and orbital ti magnetism at lamno 3/srtio 3 interfaces, Nature communications 1 (1) (2010) 1–7, doi:10.1038/ncomms1080.

[63] N. Daffé, F. Choueikani, S. Neveu, M.-A. Arrio, A. Juhin, P. Ohresser, V. Dupuis, P. Sainctavit, Magnetic anisotropies and cationic distribution in CoFe2O4 nanoparticles prepared by co-precipitation route: Influence of particle size and stoichiometry, Journal of Magnetism and Magnetic Materials 460 (2018) 243–252, doi:10.1016/j.jmmm.2018.03.041. http://www.sciencedirect.com/science/article/pii/S0304885318303561

[64] G. Vinai, A. Khare, D.S. Rana, E. Di Gennaro, B. Gobaut, R. Moroni, A.Y. Petrov, U. Scotti di Uccio, G. Rossi, F. Miletto Granozio, G. Panaccione, P. Torelli, Unraveling the magnetic properties of BiFe 0.5 Cr 0.5 O 3 thin films, APL Materials 3 (11) (2015) 116107, doi:10.1063/1.4935618.

[65] R.A. Pattrick, G. Van Der Laan, C.M.B. Henderson, P. Kuiper, E. Dudzik, D.J. Vaughan, Cation site occupancy in spinel ferrites studied by x-ray magnetic circular dichroism: developing a method for mineralogists, European Journal of Mineralogy 14 (6) (2002) 1095–1102, doi:10.1127/0935-1221/2002/0014-1095.

[66] B. Gilbert, B.H. Frazer, A. Belz, P.G. Conrad, K.H. Nealson, D. Haskel, J.C. Lang, G. Srajer, G. De Stasio, Multiple Scattering Calculations of Bonding and X-ray Absorption Spectroscopy of Manganese Oxides, The Journal of Physical Chemistry A 107 (16) (2003) 2839–2847, doi:10.1021/jp021493s. https://pubs.acs.org/doi/10.1021/jp021493s

[67] J.-S. Kang, G. Kim, H.J. Lee, D.H. Kim, H.S. Kim, J.H. Shim, S. Lee, H. Lee, J.-Y. Kim, B.H. Kim, B.I. Min, Soft x-ray absorption spectroscopy and magnetic circular dichroism study of the valence and spin states in spinel Mnfe$_2$o$_4$, Phys. Rev. B 77 (2008) 035121, doi:10.1103/PhysRevB.77.035121. https://link.aps.org/doi/10.1103/PhysRevB.77.035121

[68] E. Pollert, Influence of mn3+ ions on ordering in magnetic oxides, International Journal of Inorganic Materials 2 (6) (2000) 661–670, doi:10.1016/S1466-6049(00)00066-0. Dedicated to Prof Raveau on the occasion of his 60th Birthday, https://www.sciencedirect.com/science/article/pii/S1466604900000660

[69] Y. Ma, M.S. Molokeev, C. Zhu, S. Zhao, Y. Han, M. Wu, S. Liu, T.A. Tyson, M. Croft, M.-R. Li, Magnetic transitions in exotic perovskites stabilized by chemical and physical pressure, J. Mater. Chem. C 8 (2020) 5082–5091, doi:10.1039/C9TC06976C.

[70] J.-S. Kang, D.H. Kim, J. Hwang, E. Lee, T. Nozaki, K. Hayashi, T. Kajitani, B.-G. Park, J.-Y. Kim, B.I. Min, Phase separation in thermoelectric delafossite cufe1 xnixo2 observed by soft x-ray magnetic circular dichroism, Applied Physics Letters 99 (1) (2011) 012108, doi:10.1063/1.3609248.

[71] T. Parida, A. Karati, K. Guruvidyathri, B. Murty, G. Markandeyulu, Novel rare-earth and transition metal-based entropy stabilized oxides with spinel structure, Scripta Materialia 178 (2020) 513–517, doi:10.1016/j.scriptamat.2019.12.027. https://www.sciencedirect.com/science/article/pii/S1359646219307468

[72] A. Seko, F. Oba, I. Tanaka, Classification of spinel structures based on first-principles cluster expansion analysis, Phys. Rev. B 81 (5) (2010) 54114, doi:10.1103/PhysRevB.81.054114. https://link.aps.org/doi/10.1103/PhysRevB.81.054114

[73] D. Miracle, O. Senkov, A critical review of high entropy alloys and related concepts, Acta Mater. 122 (2017) 448–511, doi:10.1016/J.ACTAMAT.2016.08.081. https://www.sciencedirect.com/science/article/pii/S1359645416306759?via3Dihub

[74] O.F. Dippo, K.S. Vecchio, A universal configurational entropy metric for high-entropy materials, Scripta Materialia 201 (2021) 113974, doi:10.1016/j.scriptamat.2021.113974. https://www.sciencedirect.com/science/article/pii/S1359646221002542

[75] G.K. Rozenberg, Y. Amiel, W.M. Xu, M.P. Pasternak, R. Jeanloz, M. Hanfland, R.D. Taylor, Structural characterization of temperature- and pressure-induced inverse↔normal spinel transformation in magnetite, Phys. Rev. B 75 (2007) 020102, doi:10.1103/PhysRevB.75.020102. https://link.aps.org/doi/10.1103/PhysRevB.75.020102

[76] C. Zhao, F. Ding, Y. Lu, L. Chen, Y.-S. Hu, High-entropy layered oxide cathodes for sodium-ion batteries, Angewandte Chemie International Edition 59 (1) (2020) 264–269, doi:10.1002/anie.201912171.

[77] J. Wang, Y. Cui, Q. Wang, K. Wang, X. Huang, D. Stenzel, A. Sarkar, R. Azmi, T. Bergfeldt, S.S. Bhattacharya, et al., Lithium containing layered high entropy oxide structures, Scientific reports 10 (1) (2020) 1–13, doi:10.1038/s41598-020-75134-1.

[78] U.-H. Kim, G.-T. Park, P. Conlin, N. Ashburn, K. Cho, Y.-S. Yu, D.A. Shapiro, F. Maglia, S.-J. Kim, P. Lamp, C.S. Yoon, Y.-K. Sun, Cation ordered ni-rich layered cathode for ultra-long battery life, Energy Environ. Sci. 14 (2021) 1573–1583, doi:10.1039/D0EE03774E.